

1 Conductivity control via minimally invasive anti-Frenkel defects in a 2 functional oxide

3
4 Donald M. Evans^{1,*}, Theodor S. Holstad^{1,*}, Aleksander B. Mosberg^{2,*}, Didrik R. Småbråten^{1,*}, Per Erik
5 Vullum³, Anup L. Dadlani⁴, Konstantin Shapovalov⁵, Zewu Yan^{6,7}, Edith Bourret⁷, David Gao^{2,8}, Jaakko
6 Akola^{2,9}, Jan Torgersen⁴, Antonius T. J. van Helvoort², Sverre M. Selbach¹, and Dennis Meier¹

7 *The authors contributed equally

8 Email: donald.evans@ntnu.no; dennis.meier@ntnu.no

9 ¹Department of Materials Science and Engineering, Norwegian University of Science and Technology
10 (NTNU), 7491 Trondheim, Norway

11 ²Department of Physics, Norwegian University of Science and Technology (NTNU), 7491 Trondheim,
12 Norway

13 ³SINTEF Industry, 7491 Trondheim, Norway

14 ⁴Department of Mechanical and Industrial Engineering, Norwegian University of Science and
15 Technology (NTNU), 7491 Trondheim, Norway

16 ⁵Institut de Ciència de Materials de Barcelona (ICMAB-CSIC), Campus UAB, 08193 Bellaterra, Spain

17 ⁶Department of Physics, ETH Zurich, 8093 Zürich, Switzerland

18 ⁷Materials Sciences Division, Lawrence Berkeley National Laboratory, Berkeley, California 94720, USA

19 ⁸Nanolayers Research Computing LTD, 1 Granville Ct, London, N12 0HL, UK

20 ⁹Computational Physics Laboratory, Tampere University, 33014 Tampere, Finland

21
22 **Utilizing quantum effects in complex oxides, such as magnetism, multiferroicity and**
23 **superconductivity, requires atomic-level control of the material's structure and composition^{1,2}. In**
24 **contrast, the continuous conductivity changes that enable, for example, artificial oxide-based**
25 **synapses and multi-configurational devices, are driven by redox reactions and domain**
26 **reconfigurations, entailing long-range ionic migration and changes in stoichiometry or**
27 **structure^{3,4,5,6}. While both concepts hold great technological potential, combined applications seem**
28 **virtually impossible due to the mutually exclusive requirements. Here, we demonstrate a route to**
29 **overcome this limitation by controlling the conductivity in a functional oxide via electric-field**
30 **induced anti-Frenkel defects, that is, charge-neutral anion interstitial-vacancy pairs. Such defects**
31 **are generated in hexagonal Er(Mn,Ti)O₃ with nanoscale spatial precision, where they locally**
32 **enhance the electronic hopping conductivity by multiple orders of magnitude without disturbing**
33 **the ferroelectric order. We explain the observed non-volatile effects using density functional theory**
34 **and discuss its universal nature, giving a new dimension to functional oxides and the development**
35 **of multifunctional devices for next-generation nanotechnology.**

36 A continuous range of conductivity levels in oxide materials can enable innovative
37 technologies such as multilevel data storage in memristor chips and synaptic devices for neuromorphic
38 computing^{4,5,7}. Different mechanisms are now established that allow for tuning the conductivity in
39 oxides gradually and by multiple orders of magnitude⁸. For example, electric fields modify the n-type
40 conductivity in LaAlO₃-SrTiO₃ heterostructures⁹ and multiferroic (BiFeO₃)¹⁰ thin films, which has been
41 explained based on the creation and migration of positively charged oxygen vacancies ($v_{\text{O}}^{\bullet\bullet}$). In
42 addition, migration of negatively charged oxygen interstitials (O_i'') has been exploited to control the p-
43 type conductivity in hexagonal Y_{0.67}Lu_{0.33}MnO₃ single crystals¹¹. However, both the migration of $v_{\text{O}}^{\bullet\bullet}$
44 and O_i'' are aspects of the same phenomenon, that is, an electric-field driven redox reaction of a
45 transition metal oxide. While these redox reactions give the desired conductivity changes, the creation
46 of either $v_{\text{O}}^{\bullet\bullet}$ or O_i'' necessarily alters the overall stoichiometry in the host material, too, with significant
47 impact on the material's spin, charge and orbital degrees of freedom. The latter is reflected by the
48 sensitivity of oxides towards variations in stoichiometry, which can drive systems between metallic
49 and insulating states¹², stabilize superconductivity¹³, or completely suppress magnetic¹⁴ and electric
50 order^{15,16}. In general, the long-range migration and extraction/injection of ions associated with
51 currently applied redox reactions induces a net mass transport giving rise to chemical, electrostatic,
52 and strain-related gradients.^{3,5,15} This prohibits utilization in parallel with emergent electronic
53 functionalities beyond merely conductivity.

54 In order to avoid detrimental side-effects and ultimately use the full range of functional
55 properties available in oxide materials, a conceptually different approach for controlling conductivity
56 is needed. Particularly promising are stoichiometric defects as classically reported, for example, in
57 ionic fluorites¹⁶. Here, anions move from lattice sites to interstitial positions, forming entropy-
58 stabilized and charge-neutral interstitial-vacancy pairs (anti-Frenkel defects¹⁶). While in
59 electroceramics it is clear that intrinsic anti-Frenkel defects play a key role for the ionic-electronic
60 transport, their utilization for controlling conductivity in correlated oxides remains unexplored. Most

61 studies in the field of oxide electronics focus on systems from the large family of perovskite materials,
62 which are unlikely to form anti-Frenkel defects due to their rather dense crystal structure. As a
63 consequence, fundamental aspects, such as their creation, stability and impact on functionalities
64 other than mixed ionic-electronic transport, fall into largely uncharted territory.

65 In this study, we work with the ferroelectric p-type semiconductor ErMnO_3 (single-crystals,
66 see Methods) from the family of hexagonal (h-) manganites with 0.2% Ti-doping (denoted h-
67 $\text{Er}(\text{Mn},\text{Ti})\text{O}_3$ in the following). The applied Ti-doping lowers the conductivity, $\sigma_{\text{dc}}(\text{h-Er}(\text{Mn},\text{Ti})\text{O}_3) = 2.6$
68 $\times 10^{-8} \Omega^{-1} \text{cm}^{-1}$, compared to $\sigma_{\text{dc}}(\text{h-ErMnO}_3) = 2.5 \times 10^{-7} \Omega^{-1} \text{cm}^{-1}$ for the undoped sample¹⁷. Aside from
69 its semiconducting properties, h- $\text{Er}(\text{Mn},\text{Ti})\text{O}_3$ exhibits a spontaneous polarization along its [001]-axis
70 ($P \approx 5.5 \mu\text{C cm}^{-2}$), which emerges at $T_c \approx 1470 \text{ K}$ driven by a tripling of the structural unit cell^{18–20}.
71 Importantly, the structure of hexagonal manganites is about 11% less dense than the corresponding
72 orthorhombic perovskite structure, and $v_{\text{O}}^{\bullet\bullet}$ and $\text{O}_i^{\prime\prime}$ are equally important for the electronic
73 properties^{21,22}. In addition, such defects are already mobile below 200 °C, whereas cations migrate
74 only above 800 °C, which enables anion-defect driven electronic property control^{23,24}.

75 Figure 1a presents the distribution of ferroelectric 180° domains in h- $\text{Er}(\text{Mn},\text{Ti})\text{O}_3$ acquired by
76 piezoresponse force microscopy (PFM) on a sample with in-plane polarization ([110] orientation, see
77 Methods). Figure 1b shows a representative conductance map, gained by conductive atomic force
78 microscopy (cAFM) using a conducting probe-tip (curvature radius $\approx 100 \text{ nm}$) after writing a network
79 of wires with negative voltage, $U^{\text{write}} = -8 \text{ V}$, applied to the back electrode. The image is recorded with
80 a positive voltage, $U^{\text{read}} = +10 \text{ V}$, showing different wires with a width of about 100 nm and enhanced
81 conductance compared to the surrounding material. The effect is equally pronounced in $\pm P$ domains
82 and occurs on both surfaces with in-plane P (Fig. 1b) and surfaces with out-of-plane P (inset to Fig. 1c).
83 We note that this is qualitatively different from the $\text{O}_i^{\prime\prime}$ -migration-induced changes in conductance in
84 h- $\text{Y}_{0.67}\text{Lu}_{0.33}\text{MnO}_3$, which were reported to occur under comparable conditions but only on surfaces
85 with in-plane P .¹¹ Importantly, we find that the enhanced conductance of our electric-field induced

86 features persists on the time scale of years under ambient conditions (see Fig. 1c), and no signature
87 of degradation is observed up to 105 °C (Supplementary Fig. S1). A reset to the original state is possible
88 by annealing at 300 °C, reflecting a barrier for stability in the order of 0.035 to 0.050 eV (Fig. S2).
89 Furthermore, and in contrast to previous AFM-written conducting nano-features in $\text{LaAlO}_3\text{-SrTiO}_3$ ^{9,25}
90 that rely on hydrogen (H^+) penetration, our structures are robust against solvents, such as acetone,
91 ethanol, and methanol. In fact, we do not observe qualitative differences between writing conducting
92 features in air (ambient) and under nitrogen atmosphere (Fig. S3), which discards H^+ penetration as
93 the driving force behind the change in conductivity. The conclusion that neither only O_i'' nor H^+ is
94 responsible for the enhanced conductance is corroborated by time- and voltage-dependent studies
95 (Fig. S4), as well as local transport measurements (Fig. S5), which cannot be explained by only one
96 type of defect. To quantify the induced changes in conductivity and to analyse the influence of the
97 polarity (+ or -) and size of the applied voltage, we draw a series of boxes (see inset to Fig. 1d),
98 systematically varying the write voltage U^{write} from -10 V to +10 V. The impact of the varying U^{write} is
99 then monitored by cAFM scans taken with a positive voltage of +10 V. The results are summarized in
100 Fig. 1d, which shows the averaged measured current, I^{read} , as function of U^{write} . Figure 1d reveals that
101 I^{read} depends on the polarity of the write voltage: for negative voltages exceeding -5 V, we observe an
102 increase in the conductance by about three orders of magnitude. In contrast, positive voltages do not
103 lead to an increase in the conductance, consistent with the formation of a Schottky barrier at the tip-
104 sample interface.^{11,26} The latter is also confirmed by separate experiments at higher voltages up to
105 +60 V (see Fig. S6). Thus, the experiments demonstrate that conducting features can be written with
106 negative voltages ($U^{\text{write}} \lesssim -5$ V) and read-out by positive voltages ($0 < U^{\text{read}} \lesssim +60$ V). By writing
107 features of different shapes (wires and dots), we can achieve an enhancement of up to four orders of
108 magnitude in I^{read} without significant changes in surface topography (see Supplementary Fig. S7 and
109 S8). The data demonstrates that localized electric fields can enhance the conductance in h-Er(Mn,Ti)O_3
110 by up to four orders of magnitude; the changes are durable, resistant to moderate heating and
111 chemical solvents, and can be induced with nanometer spatial precision.

112 To understand the origin of the enhanced conductance, we investigate how the effect evolves
113 within the bulk. Figure 2a and inset show a comparison of scanning electron microscopy (SEM) and
114 cAFM images from the same area, revealing an elliptically shaped bright area that has been written
115 with $U^{\text{write}} = -60$ V applied for 5 s. A comparison of the SEM and cAFM data shows that bright contrast
116 in SEM correlates with high conductivity. This correlation allows us to evaluate how the electric-field
117 induced changes protrude into the depth of the sample based on SEM images. For this purpose, we
118 take a cross-sectional images from the region of interest (Fig. 2b), using a dual beam focused ion beam
119 (FIB)-SEM (see Methods). Consistent with our AFM data (Fig. S8), the cross-sectional SEM images show
120 no significant change in surface topography. Instead, Figure 2b reveals that the region of enhanced
121 conductance extends more than $0.5 \mu\text{m}$ into the depth of the sample. A schematic 3D reconstruction
122 of the conducting area based on the SEM data is presented in Fig. 2c. This distribution is consistent
123 with the anisotropic behaviour observed in the electronic transport²⁷ and the ionic mobility in the
124 hexagonal manganites (Supplementary Fig. S9), indicating that the changes that give rise to enhanced
125 conductance are a bulk phenomenon rather than a surface effect.

126 To test for related structural modifications in the bulk, we take high-angle annular dark field
127 scanning transmission electron microscopy (HAADF-STEM) lattice images inside and away from the
128 conducting region in Fig. 2b. Figure 2d and 2e present HAADF-STEM scans viewed down the $[\bar{1} 0 0]$
129 direction, comparing the electrically modified region to the as-grown structure, respectively. The
130 images represent the typical up-up-down pattern of Er atoms²⁸, separated by layers of Mn atoms.
131 Interestingly, both real and reciprocal space investigations show no differences in positions between
132 the two regions (see Fig. 2d and 2e, and insets). In particular, when analysing the arrangement of Er
133 atoms, we find no statistically significant decrease in Er displacement within the conductive region, or
134 modification of the unit cell size (Supplementary Fig. S10), suggesting that the driving mechanism for
135 enhanced conductivity is due to subtle effects related to the local electronic structure. Furthermore,
136 as the improper electric polarization in $\text{h-Er}(\text{Mn,Ti})\text{O}_3$ arises from the Er displacement^{29–32}, its

137 robustness demonstrates that the orientation and magnitude of the ferroelectric order is unaffected
138 by the electric-field induced increase in conductance (Fig. 2a,b).

139 We next analyse the electronic structure at the local scale, using electron energy-loss
140 spectroscopy (EELS). Figure 3a displays averaged EELS spectra showing the Mn $L_{2,3}$ -edge in the bulk
141 (blue) and the modified conducting region (yellow). A comparison of the EELS data reveals changes in
142 spectral weight, whereas the L_3/L_2 white-line intensity ratio remains constant, suggesting that the net
143 Mn oxidation state is preserved. We demonstrate the reproducibility of this subtle effect by recording
144 EELS spectra at the Mn $L_{2,3}$ -edge from a second line scan in different positions, which leads to
145 qualitatively equivalent results (see Fig. S11). To evaluate the detected change, we follow the
146 approach used in ref. [33-37] and fit the full Mn $L_{2,3}$ -edge with three spectra, corresponding to Mn^{2+} and
147 Mn^{4+} spectra from literature³⁷ and experimental reference spectra recorded away from the
148 conducting region. This procedure allows for quantifying relative changes with respect to the bulk
149 even without knowing the exact defect density in the as-grown state (note that bulk $h\text{-Er}(\text{Mn,Ti})\text{O}_3$
150 displays p-type conductivity, which implies the presence of O_i'' , Fig. S5). We find that linear
151 combinations of two spectra (bulk and Mn^{2+} , or bulk and Mn^{4+}) alter the peak form and L_3/L_2 white-
152 line intensity ratio, thus excluding the possibility making it unlikely that only one defect type (either
153 $v_O^{\bullet\bullet}$ or O_i'') is responsible for the experimentally observed change in spectral weight (see
154 Supplementary Fig. S11 and S12 for details). In contrast, assuming an equal concentration of Mn^{2+} and
155 Mn^{4+} , we can reproduce the averaged EELS spectra for the Mn $L_{2,3}$ -edge in the conducting regime (red
156 lines in Fig. 3(a), Fig. S10 and S12), suggesting a coexistence of $v_O^{\bullet\bullet}$ and O_i'' . The latter is consistent with
157 the formation of $(v_O^{\bullet\bullet}, O_i'')$ defect pairs, i.e., anti-Frenkel defects¹⁶. On the basis of our fits, we calculate
158 an increase of about 3.25 ± 0.5 % in the concentration of Mn^{4+} and Mn^{2+} relative to the bulk,
159 corresponding to about one anti-Frenkel defect for every ninth unit cells (Supplementary Fig. S12).

160 To find additional evidence, we consider EELS spectra taken at the O K-edge in the bulk (Fig.
161 3b) and in the conducting region (Fig. 3c) and apply the *ab initio* self-consistent multiple-scattering

162 code FEFF³⁸ to analyse emergent site-specific differences for the four symmetrically inequivalent
163 oxygen positions¹⁹ in h-Er(Mn,Ti)O₃ (see inset to Fig. 3a). Representative calculated spectra for apical
164 (O1 and O2) and planar (O3) oxygen are given as insets to Fig. 3b and c, respectively. For the bulk, the
165 spectra calculated for apical oxygen in an oxygen stoichiometric system adequately replicate the main
166 features of the O K-edge, labelled ① to ⑤ (an overview of all oxygen spectra is given in Fig. S13). In
167 contrast, in the conducting region (yellow in Fig. 3c) the O K-edge shows several differences compared
168 to the bulk, including the emergence of a distinct peak at about 537 eV, which can no longer be
169 explained based on apical oxygen alone. At this energy, however, a peak is present in the calculated
170 spectra for planar oxygen (O3, black line), which is expected to have an increased contribution in the
171 presence of anti-Frenkel defects due to changes in the oxygen bond angle (see inset to Fig. 3c for an
172 illustration). Although the O K-edge results are in tune with the data gained at the Mn L_{2,3}-edge and
173 consistent with the formation of anti-Frenkel defects, from the spectroscopy data alone one cannot
174 unambiguously conclude a coexistence of both $v_{\text{O}}^{\bullet\bullet}$ and $\text{O}_i^{\prime\prime}$. Direct evidence of this coexistence is
175 provided, however, by the time- and voltage-dependent study in Fig. S4, showing a separation of
176 positively ($v_{\text{O}}^{\bullet\bullet}$) and negatively ($\text{O}_i^{\prime\prime}$) charged defects under longer exposure to electric fields.

177 To develop a microscopic model, we apply first principles calculations based on density
178 functional theory (DFT) using the isostructural compound h-YMnO₃ as model system (Methods;
179 analogous to ref. [33] the calculations are performed for h-YMnO₃, which is structurally and
180 electronically similar to h-ErMnO₃, but the absence of f-electrons simplifies the DFT description). We
181 find that $\text{O}_i^{\prime\prime}$ (locally contracting the lattice²¹) and $v_{\text{O}}^{\bullet\bullet}$ (locally expanding the lattice³⁹) are structurally
182 screened and, hence, do not recombine when they are more than ≈ 6 Å apart. Instead, at $T = 0$ K, they
183 form an electrically compensated meta-stable anti-Frenkel defect ($v_{\text{O}}^{\bullet\bullet}, \text{O}_i^{\prime\prime}$) as sketched in Fig. 4a (see
184 Supplementary Notes and Supplementary Figs. S14 and S15 for details). To gain insight into the defect
185 structure at finite temperature and analyse its stability, we perform molecular dynamic (MD)
186 simulations at 300 K, 573 K, and 1000 K (see Supplementary Information). The MD simulations reveal

187 that the system can slightly lower its energy by forming O_i'' -dimers, subtly modifying the basic anti-
188 Frenkel defect structure in Fig. 4a (see Fig. S16 for an illustration). The modified anti-Frenkel defect
189 exhibits a DOS comparable to Fig. 4c and, importantly, does not recombine at 300 K and 573 K within
190 5 ps and 10 ps trajectories, respectively. In contrast, at 1000 K we observe recombination within 3 ps,
191 confirming that recombination occurs at sufficiently high temperature.

192 The higher conductance in regions with enhanced anti-Frenkel defect density can be
193 understood from the calculated electronic density of states (DOS) and the corresponding simplified
194 band structure in Fig. 4c (see Fig. S17 for the site-specific DOS). In general, electrical transport in h-
195 $Er(Mn,Ti)O_3$ occurs via hopping conductivity, reported as Poole-Frenkel conduction¹⁷, and the same
196 mechanism is observed in the modified region (Fig. S18). Figure 4c shows that both the number of
197 charge carriers and defect sites available for hopping increase, explaining the observed higher hopping
198 conductivity. The electron-hole pairs associated with anti-Frenkel defects may recombine and give rise
199 to an electrically uncompensated charge state of the anti-Frenkel defect. However, the latter is
200 energetically costly so that new charge carriers would be created to replace the missing electron-hole
201 pair and move the system back to equilibrium (Fig. S15).

202 The electric-field induced anti-Frenkel defects studied in this work thus enable minimally
203 invasive and non-volatile conductivity control with nanoscale spatial precision. Importantly, the
204 emergence of parasitic chemical, electrostatic, and strain-related gradients associated with
205 conventional approaches is avoided and the material's overall stoichiometry is preserved. Anti-Frenkel
206 defects can be applied in any system that can stably compensate multiple oxygen stoichiometries,
207 such as the families of hexagonal rare-earth gallates and indates⁴⁰, hexaferrite⁴¹, fluorites⁴²,
208 Ruddlesdon-Popper⁴³ systems as well as tungsten bronzes. Here, – analogous to the hexagonal
209 manganites – their controlled creation via electric fields is likely, allowing to increase the density of
210 defect sites and enhance hopping conductivity. With this, a new generation of multifunctional oxides
211 becomes possible in which multilevel conductivity control can be utilized in parallel with phenomena

212 such as ferroelectricity, magnetism, and superconductivity without changing the electronic
213 interactions that control them.

214

215 **References**

- 216 1. Hwang, H. Y. *et al.* Emergent phenomena at oxide interfaces. *Nat. Mater.* **11**, 103–113 (2012).
- 217 2. Ramesh, R. & Schlom, D. G. Creating emergent phenomena in oxide superlattices. *Nat. Rev.*
218 *Mater.* **4**, 257–268 (2019).
- 219 3. Kumar, A., Ciucci, F., Morozovska, A. N., Kalinin, S. V. & Jesse, S. Measuring oxygen
220 reduction/evolution reactions on the nanoscale. *Nat. Chem.* **3**, 707–713 (2011).
- 221 4. Seok Jeong, D., Kim, I., Ziegler, M. & Kohlstedt, H. Towards artificial neurons and synapses: A
222 materials point of view. *RSC Adv.* **3**, 3169–3183 (2013).
- 223 5. Ielmini, D. & Wong, H. S. P. In-memory computing with resistive switching devices. *Nat.*
224 *Electron.* **1**, 333–343 (2018).
- 225 6. Chanthbouala, A. *et al.* A ferroelectric memristor. *Nat. Mater.* **11**, 860 (2012).
- 226 7. Del Valle, J., Ramírez, J. G., Rozenberg, M. J. & Schuller, I. K. Challenges in materials and
227 devices for resistive-switching-based neuromorphic computing. *J. Appl. Phys.* **124**, 211101
228 (2018).
- 229 8. Lee, J. S., Lee, S. & Noh, T. W. Resistive switching phenomena: A review of statistical physics
230 approaches. *Appl. Phys. Rev.* **2**, 31303 (2015).
- 231 9. Cen, C. *et al.* Nanoscale control of an interfacial metal–insulator transition at room
232 temperature. *Nat. Mater.* **7**, 298 (2008).
- 233 10. Du, N. *et al.* Field-Driven Hopping Transport of Oxygen Vacancies in Memristive Oxide

- 234 Switches with Interface-Mediated Resistive Switching. *Phys. Rev. Appl.* **10**, 54025 (2018).
- 235 11. Wang, X. *et al.* Anisotropic resistance switching in hexagonal manganites. *Phys. Rev. B* **99**,
236 054106 (2019).
- 237 12. Nagarajan, L. *et al.* A chemically driven insulator-metal transition in non-stoichiometric and
238 amorphous gallium oxide. *Nat. Mater.* **7**, 391–398 (2008).
- 239 13. Cava, R. J. *et al.* Oxygen stoichiometry, superconductivity and normal-state properties of
240 $\text{YBa}_2\text{Cu}_3\text{O}_{7-\delta}$. *Nature* **329**, 423–425 (1987).
- 241 14. Zhao, J. *et al.* Lattice and magnetic structures of PrFeAsO , $\text{PrFeAsO}_{0.85}\text{F}_{0.15}$, and $\text{PrFeAsO}_{0.85}$.
242 *Phys. Rev. B* **78**, 132504 (2008).
- 243 15. Kalinin, S. V., Jesse, S., Tselev, A., Baddorf, A. P. & Balke, N. The role of electrochemical
244 phenomena in scanning probe microscopy of ferroelectric thin films. *ACS Nano* **5**, 5683–5691
245 (2011).
- 246 16. Joachim Maier. *Physical Chemistry of Ionic Materials. Ions and Electrons in Solids* (Wiley,
247 2004).
- 248 17. Holstad, T. S. *et al.* Electronic bulk and domain wall properties in B-site doped hexagonal
249 ErMnO_3 . *Phys. Rev. B* **97**, 85143 (2018).
- 250 18. Chae, S. C. *et al.* Direct observation of the proliferation of ferroelectric loop domains and
251 vortex-antivortex pairs. *Phys. Rev. Lett.* **108**, 167603 (2012).
- 252 19. Van Aken, B. B., Palstra, T. T. M., Filippetti, A. & Spaldin, N. A. The origin of ferroelectricity in
253 magnetoelectric YMnO_3 . *Nat. Mater.* **3**, 164–170 (2004).
- 254 20. Han, M.-G. *et al.* Ferroelectric Switching Dynamics of Topological Vortex Domains in a
255 Hexagonal Manganite. *Adv. Mater.* **25**, 2415–2421 (2013).
- 256 21. Skjærø, S. H. *et al.* Interstitial oxygen as a source of p-type conductivity in hexagonal

- 257 manganites. *Nat. Commun.* **7**, 13745 (2016).
- 258 22. Skjærvø, S. H., Småbråten, D. R., Spaldin, N. A., Tybell, T. & Selbach, S. M. Oxygen vacancies in
259 the bulk and at neutral domain walls in hexagonal YMnO₃. *Phys. Rev. B* **98**, 184102 (2018).
- 260 23. Remsen, S. & Dabrowski, B. Synthesis and oxygen storage capacities of hexagonal Dy_{1-x}Y
261 _xMnO_{3+δ}. *Chem. Mater.* **23**, 3818–3827 (2011).
- 262 24. Bergum, K. *et al.* Synthesis, structure and magnetic properties of nanocrystalline YMnO₃. *Dalt.*
263 *Trans.* **40**, 7583–7589 (2011).
- 264 25. Bi, F. *et al.* ‘Water-cycle’ mechanism for writing and erasing nanostructures at the
265 LaAlO₃/SrTiO₃ interface. *Appl. Phys. Lett.* **97**, 173110 (2010).
- 266 26. Schaab, J. *et al.* Electrical half-wave rectification at ferroelectric domain walls. *Nat.*
267 *Nanotechnol.* **13**, 1028–1034 (2018).
- 268 27. Katsufuji, T. *et al.* Dielectric and magnetic anomalies and spin frustration in hexagonal RMnO₃
269 (*R* = Y, Yb, and Lu). *Phys. Rev. B* **64**, 104419 (2001).
- 270 28. Zhang, Q. H. *et al.* Direct observation of interlocked domain walls in hexagonal RMnO₃
271 (*R*=Tm, Lu). *Phys. Rev. B* **85**, 20102 (2012).
- 272 29. Holtz, M. E. *et al.* Topological Defects in Hexagonal Manganites: Inner Structure and
273 Emergent Electrostatics. *Nano Lett.* **17**, 5883–5890 (2017).
- 274 30. Fennie, C. J. & Rabe, K. M. Ferroelectric transition in YMnO₃ from first principles. *Phys. Rev. B*
275 **72**, 100103 (2005).
- 276 31. Artyukhin, S., Delaney, K. T., Spaldin, N. A. & Mostovoy, M. Landau theory of topological
277 defects in multiferroic hexagonal manganites. *Nat. Mater.* **13**, 42 (2013).
- 278 32. Cano, A. Hidden order in hexagonal RMnO₃ multiferroics (*R*=Dy -Lu, In, Y, and Sc). *Phys. Rev. B*
279 **89**, 214107 (2014).

- 280 33. Mundy, J. A. *et al.* Functional electronic inversion layers at ferroelectric domain walls. *Nat.*
281 *Mater.* **16**, 622 (2017).
- 282 34. Tan, H., Verbeeck, J., Abakumov, A. & Van Tendeloo, G. Oxidation state and chemical shift
283 investigation in transition metal oxides by EELS. *Ultramicroscopy* **116**, 24–33 (2012).
- 284 35. Nishida, S. *et al.* Effect of local coordination of Mn on Mn-L_{2,3} edge electron energy loss
285 spectrum. *J. Appl. Phys.* **114**, 54906 (2013).
- 286 36. Loomer, D. B., Al, T. A., Weaver, L. & Cogswell, S. Manganese valence imaging in Mn minerals
287 at the nanoscale using STEM-EELS. *Am. Mineral.* **92**, 72–79 (2007).
- 288 37. Garvie, L. A. J. & Craven, A. J. High-resolution parallel electron energy-loss spectroscopy of
289 Mn L_{2,3}-edges in inorganic manganese compounds. *Phys. Chem. Miner.* **21**, 191–206 (1994).
- 290 38. Rehr, J. J., Kas, J. J., Vila, F. D., Prange, M. P. & Jorissen, K. Parameter-free calculations of X-
291 ray spectra with FEFF9. *Phys. Chem. Chem. Phys.* **12**, 5503–5513 (2010).
- 292 39. Overton, A. J., Best, J. L., Saratovsky, I. & Hayward, M. A. Influence of topotactic reduction on
293 the structure and magnetism of the multiferroic YMnO₃. *Chem. Mater.* **21**, 4940–4948 (2009).
- 294 40. Griffin, S. M., Reidulff, M., Selbach, S. M. & Spaldin, N. A. Defect Chemistry as a Crystal
295 Structure Design Parameter: Intrinsic Point Defects and Ga Substitution in InMnO₃. *Chem.*
296 *Mater.* **29**, 2425–2434 (2017).
- 297 41. Zhang, X., Zhang, Y., Yue, Z. & Zhang, J. Influences of sintering atmosphere on the magnetic
298 and electrical properties of barium hexaferrites. *AIP Adv.* **9**, 085129 (2019).
- 299 42. Keeton, S. C. & Wilson, W. D. Vacancies, interstitials, and rare gases in fluorite structures.
300 *Phys. Rev. B* **7**, 834–843 (1973).
- 301 43. Boulahya, K., Muñoz-Gil, D., Gómez-Herrero, A., Azcondo, M. T. & Amador, U.
302 Eu₂SrCo_{1.5}Fe_{0.5}O₇ a new promising Ruddlesden-Popper member as a cathode component for

- 303 intermediate temperature solid oxide fuel cells. *J. Mater. Chem. A* **7**, 5601–5611 (2019).
- 304 44. Yan, Z. *et al.* Growth of high-quality hexagonal ErMnO_3 single crystals by the pressurized
305 floating-zone method. *J. Cryst. Growth* **409**, 75–79 (2015).
- 306 45. Jones, L. *et al.* Smart Align—a new tool for robust non-rigid registration of scanning
307 microscope data. *Adv. Struct. Chem. Imaging* **1**, 8 (2015).
- 308 46. Nord, M., Vullum, P. E., MacLaren, I., Tybell, T. & Holmestad, R. Atomap: a new software tool
309 for the automated analysis of atomic resolution images using two-dimensional Gaussian
310 fitting. *Adv. Struct. Chem. Imaging* **3**, 9 (2017).
- 311 47. Blöchl, P. E. Projector augmented-wave method. *Phys. Rev. B* **50**, 17953–17979 (1994).
- 312 48. Kresse, G. & Furthmüller, J. Efficient iterative schemes for ab initio total-energy calculations
313 using a plane-wave basis set. *Phys. Rev. B* **54**, 11169–11186 (1996).
- 314 49. Kresse, G. & Joubert, D. From ultrasoft pseudopotentials to the projector augmented-wave
315 method. *Phys. Rev. B* **59**, 1758–1775 (1999).
- 316 50. Medvedeva, J. E., Anisimov, V. I., Korotin, M. A., Mryasov, O. N. & Freeman, A. J. Effect of
317 Coulomb correlation and magnetic ordering on the electronic structure of two hexagonal
318 phases of ferroelectromagnetic YMnO_3 . *J. Phys. Condens. Matter* **12**, 4947–4958 (2001).
- 319 51. Gibbs, A. S., Knight, K. S. & Lightfoot, P. High-temperature phase transitions of hexagonal
320 YMnO_3 . *Phys. Rev. B* **83**, 94111 (2011).
- 321 52. Degenhardt, C., Fiebig, M., Fröhlich, D., Lottermoser, T. & Pisarev, R. V. V. Nonlinear optical
322 spectroscopy of electronic transitions in hexagonal manganites. *Appl. Phys. B* **73**, 139–144
323 (2001).
- 324 53. Perdew, J. P. *et al.* Restoring the Density-Gradient Expansion for Exchange in Solids and
325 Surfaces. *Phys. Rev. Lett.* **100**, 136406 (2008).

- 326 54. Dudarev, S. L., Botton, G. A., Savrasov, S. Y., Humphreys, C. J. & Sutton, A. P. Electron-energy-
327 loss spectra and the structural stability of nickel oxide: An LSDA+U study. *Phys. Rev. B* **57**,
328 1505–1509 (1998).
- 329 55. Murphy, S. T. & Hine, N. D. M. Anisotropic charge screening and supercell size convergence of
330 defect formation energies. *Phys. Rev. B* **87**, 94111 (2013).
- 331 56. Rehr, J. J. *et al.* Ab initio theory and calculations of X-ray spectra. *Comptes Rendus Phys.* **10**,
332 548–559 (2009).

333

334 **Acknowledgements** The authors thank Tor Grande for fruitful discussions. DRS and SMS were
335 supported by the Research Council of Norway (project number 231430/F20 and 275139) and
336 acknowledge UNINETT Sigma2 (Project no. NN9264K and ntnu243) for providing the computational
337 resources. ABM was supported by NTNU's Enabling technologies: Nanotechnology. The Research
338 Council of Norway is acknowledged for the support to the Norwegian Micro- and Nano-Fabrication
339 Facility, NorFab, project number 245963/F50 and Norwegian Centre for Transmission Electron
340 Microscopy, NORTEM, Grant No. 197405. ALD was funded by the Norwegian Research Council under
341 project number 274459 Translate. ZY and EB were supported by the U.S. Department of Energy, Office
342 of Science, Basic Energy Sciences, Materials Sciences and Engineering Division under Contract No. DE-
343 AC02-05-CH11231 within the Quantum Materials program-KC2202. DM thanks NTNU for support
344 through the Onsager Fellowship Programme and NTNU Stjerneprogrammet.

345

346 **Author contributions** DME coordinated the project and lead the scanning probe microscopy work
347 together with TSH, both supervised by DM. ABM conducted the FIB and SEM work under supervision
348 of AvH. PEV, AvH, ABM, conducted TEM and together with TSH and DME analyzed the TEM and EELS
349 data. DRS performed the DFT calculations and ALD simulated the EELS spectra supervised by SMS and

350 JT, respectively. KS modelled the defect segregation in electric fields. ZY and EB provided the materials
351 and DG and JA supported the study with image charge and potential alignment correction simulations
352 for charged defects in periodic boundary conditions. DME and DM wrote the manuscript. All authors
353 discussed the results and contributed to the final version of the manuscript.

354

355 **Data availability** The data that support the plots within this paper and other findings of this study are
356 available from the corresponding author upon reasonable request.

357

358 **Additional information** Supplementary information is available for this paper at <https://...> Reprints
359 and permission information is available online at www.nature.com/reprints. Correspondence and
360 requests for materials should be addressed to DME and DM.

361

362

363

364

365

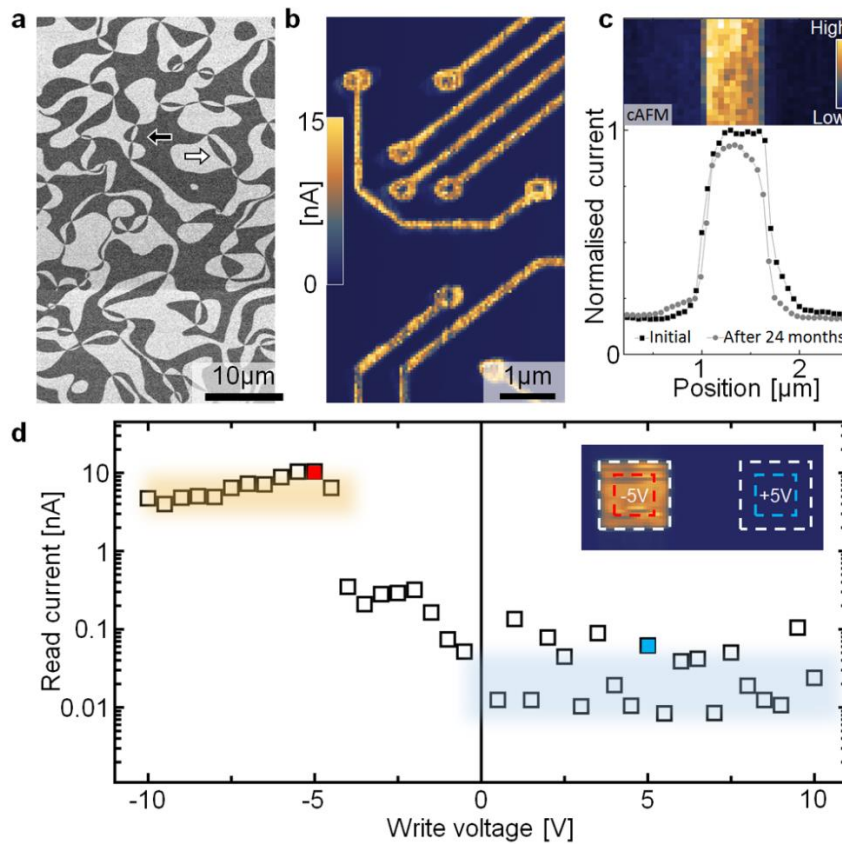
366

367

368

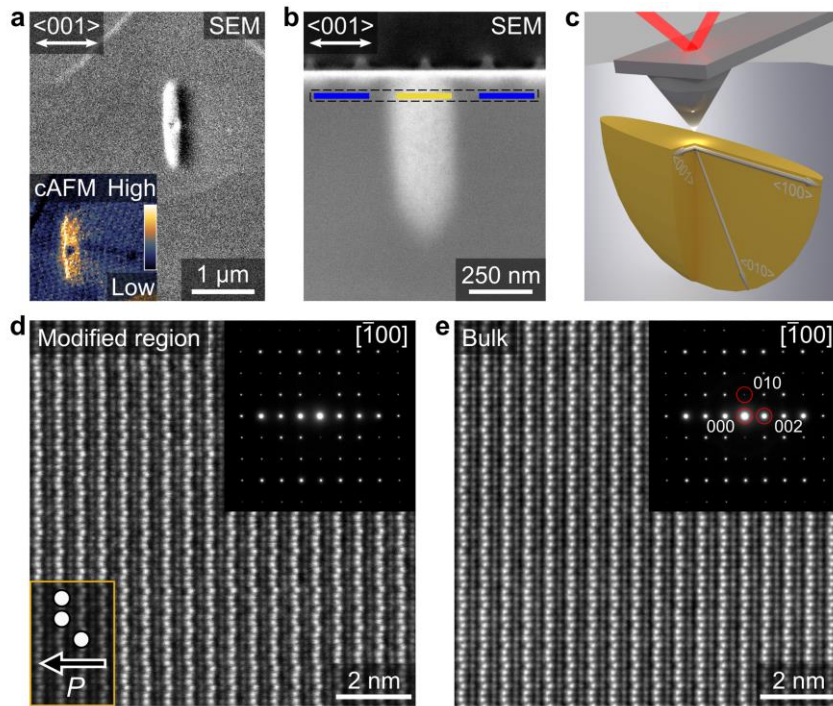
369

370



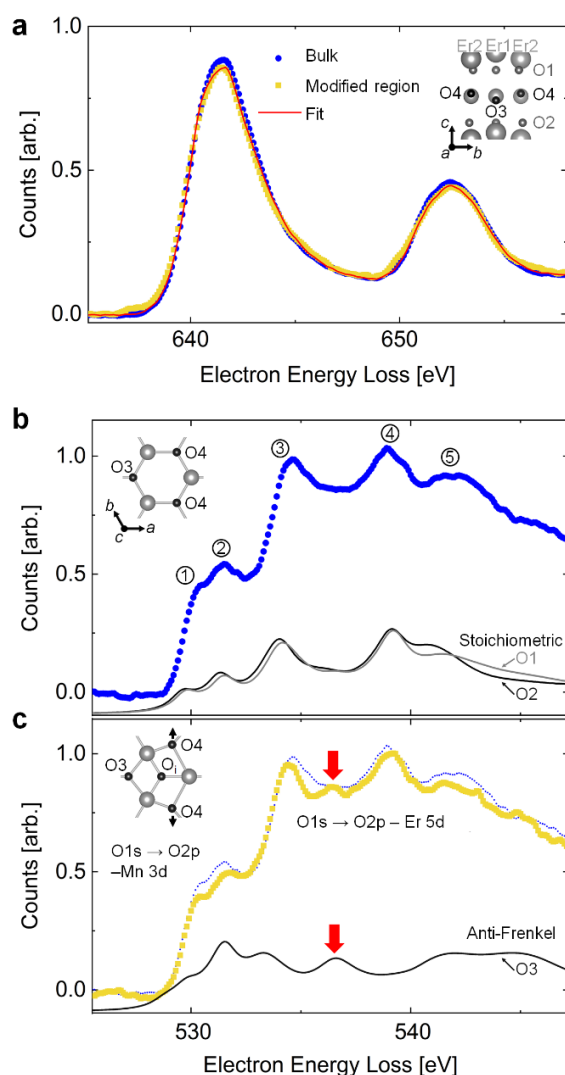
372

373 **Figure 1 | Local conductivity control in hexagonal h-Er(Mn,Ti)O₃.** **a**, Piezoresponse force microscopy
 374 (PFM, in-plane contrast) image, showing the characteristic distribution of ferroelectric domains.
 375 Arrows indicate the polarisation direction (dark, $-P$ and bright, $+P$). **b**, Conductive atomic force
 376 microscopy (cAFM) scan showing conducting nano-wires (bright) on a less conducting background of
 377 both $-P$ and $+P$ domains similar to **a**. The image is gained with a positive bias ($U^{\text{read}} = +10$ V) after
 378 writing wires with a negative bias of ($U^{\text{write}} = -8$ V). **Voltages are applied to the back electrode.** **c**,
 379 Normalised current recorded on a conducting bar right after writing it on a sample with out-of-plane
 380 P and, again, 24 months later ($U^{\text{read}} = +12$ V, $U^{\text{write}} = -21$ V). The profiles are gained from cAFM images
 381 as shown in the inset by averaging over multiple cross sections. The curves are offset so that the
 382 background current away from the conducting feature aligns. The data reflects the long-term stability
 383 of the electric-field induced conducting features in h-Er(Mn,Ti)O₃. **d**, Average current measured at
 384 $U^{\text{read}} = +10$ V from a series of 1×1 μm boxes written with voltages between -10 V and $+10$ V.
 385 Representative spatially resolved cAFM data for boxes written with ± 5 V are shown in the inset. White
 386 dashed lines frame the boxes, whereas coloured dashed lines mark the areas (0.5×0.5 μm) over which
 387 the current is averaged to quantify the read current.



388

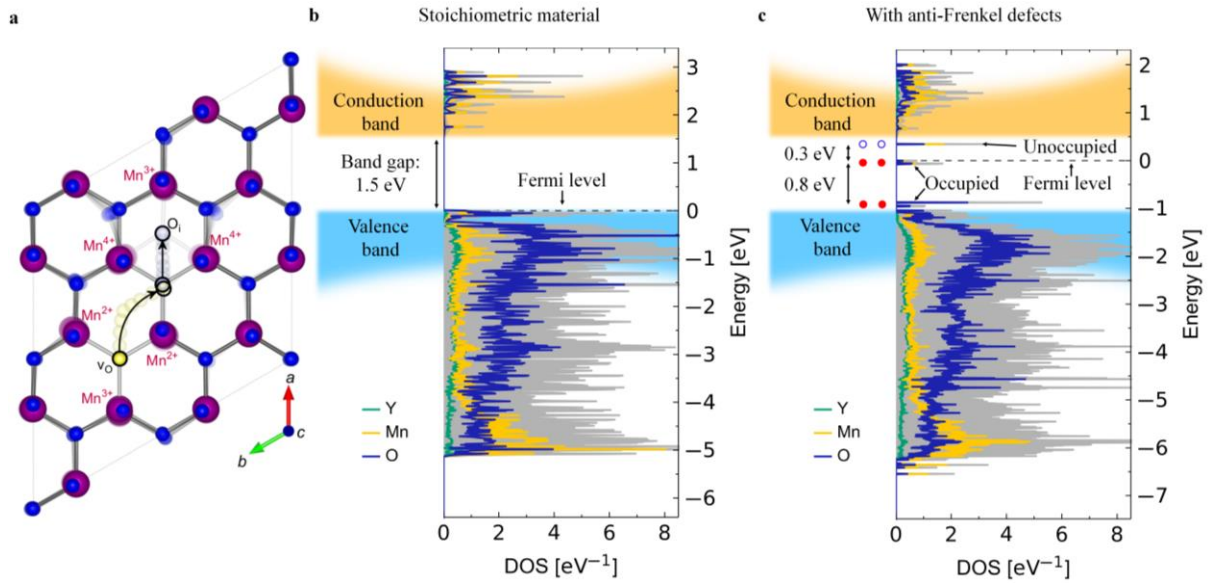
389 **Figure 2 | Morphology and structure of electric-field induced conducting features.** **a**, Top-down SEM
 390 and cAFM (inset, $U^{\text{read}} = +45$ V) image of an elliptically shaped conducting region (bright), generated
 391 by applying $U^{\text{write}} = -60$ V for 5 s, while keeping the probe tip stationary probe. The white arrow
 392 indicates the ferroelectric axis ($P \parallel \langle 001 \rangle$). **b**, SEM image of a FIB cross-section from **a**, revealing how
 393 the conducting feature protrudes into the bulk of h-Er(Mn,Ti)O₃ and showing where, in the final TEM
 394 lamella, the EELS line scan for Fig. 3 is taken (blue and yellow represent the bulk and electrically
 395 modified region, respectively). **c**, 3D sketch representing the cAFM induced conducting feature and
 396 the shape dependence on crystallographic axes based on the cross section in **b** and cross sections of
 397 equivalent dots taken in perpendicular directions. **d**, HAADF-STEM image from the high conductive
 398 region seen in **b**, viewed along the $P6_3cm$ $[\bar{1}00]$ zone axis, with $\tau/\lambda = 0.40 \pm 0.02$. The brighter Er atomic
 399 positions show the characteristic up-up-down displacement as discussed in ref. [29] and the arrow in
 400 the inset shows how this links to the ferroelectric polarisation P . **e**, HAADF-STEM image taken in the
 401 unmodified bulk region. The analysis of the crystal lattice in **d** and **e** reveals no measurable differences,
 402 reflecting that the atomic scale structure and, hence, the ferroelectric polarisation, are unaffected by
 403 the electric-field induced change in conductivity. Insets in **(d, e)** show selected area electron diffraction
 404 (SAED) patterns of the corresponding regions.



405

406 **Figure 3 | Comparison of the electronic structure in as-grown and electrically modified regions. a,**
 407 Blue and yellow data points represent EELS spectra of the Mn $L_{2,3}$ edge in h-Er(Mn,Ti)O₃ taken in the
 408 bulk and the modified conducting region, respectively ($t/\lambda = 0.40 \pm 0.02$). The red line is a fit to the Mn
 409 $L_{2,3}$ edge in the conducting region based on a linear combination of spectra corresponding to Mn²⁺,
 410 Mn³⁺ and Mn⁴⁺ valence states with 3.75 % Mn²⁺ and 3.75 % Mn⁴⁺, that is, approximately one anti-
 411 Frenkel defect in every nine unit cells. The inset shows the symmetry inequivalent Er and O positions.
 412 **b,** Data points present the O K-edge in the bulk. Grey and black lines are calculated spectra for apical
 413 oxygen (O1 and O2), respectively, in a stoichiometric crystal. **c,** Yellow points present the O K-edge in
 414 the region with enhanced conductivity (the bulk spectrum (blue) is shown for reference). The black
 415 line is the calculated spectrum for planar oxygen (O3) in the presence of anti-Frenkel defects as
 416 sketched in the inset. Transitions are labelled according to the projected density of states (pDOS,
 417 Supplementary Fig. S13b). Red arrows indicate a peak at about 537 eV, which is characteristic for
 418 contributions from planar oxygen. All EELS spectra are taken on the same single line scan with even
 419 thickness and are spatially averaged over the regions indicated by the blue and yellow lines in Fig. 2b.

420



421

422 **Figure 4 | Anti-Frenkel defects and electronic density of states.** **a**, Formation of an anti-Frenkel defect
 423 in a 120 atom supercell. A planar lattice oxygen (yellow) is migrating from its lattice site into another
 424 planar oxygen lattice site (grey), which in turn is nudged into an interstitial site, resulting in the
 425 formation of an anti-Frenkel defect. The resulting local charge compensation of the constituting O_i''
 426 and $v_O^{\bullet\bullet}$ are labelled Mn^{4+} and Mn^{2+} , respectively. **b**, Total (grey) and atomic electronic density of states
 427 (DOS) for a stoichiometric 270 atom h-YMnO₃ supercell with key features schematically highlighted
 428 (valence band – light blue, conduction band – dark yellow). **c**, Same calculation for a 270 atom h-
 429 YMnO₃ supercell containing one anti-Frenkel defect, that is, one anti-Frenkel defect in every nine unit
 430 cells or, equivalently, 3.70 % Mn atoms in the Mn^{4+} state and 3.70 % in the Mn^{2+} state. Red and blue
 431 spheres in **c** schematically illustrate occupied and unoccupied defect states within the band gap.

432

433

434

435

436

437

438 **Methods**

439 **Samples** High-quality single crystals are grown by the pressurised floating-zone method⁴⁴ and
440 different samples are oriented by Laue diffraction and cut with thicknesses of $\approx 0.5 - 1$ mm. The
441 surfaces are chemo-mechanically polished with silica slurry to give a root-mean-square roughness of
442 about 1 nm.

443 **Scanning probe microscopy** The SPM measurements are recorded using a NT-MDT NTEGRA Prima
444 SPM. For all the cAFM scans we used TipsNano DCP20 probes with the voltage applied to the back of
445 the sample. For the PFM scans we used Asylec-01-R2 Ti/Ir probes with an AC voltage amplitude of 10
446 V applied to the back of the sample.

447 **Transmission electron microscopy** TEM specimens are prepared from the middle of the conductive
448 region using a Thermo Fisher Scientific G4 UX DualBeam FIB (Focused Ion Beam). In-situ lift-out is done
449 with backside milling and a final polishing voltage of 2 kV. (S)TEM is performed with a double Cs
450 corrected cold FEG JEOL ARM 200FC, operated at 200 kV and equipped with a Quantum ER GIF. High
451 resolution high-angle-annular-dark-field scanning transmission electron microscopy (HAADF STEM)
452 images are taken with a spatial resolution of 78 pm. The energy resolution, as determined by the
453 FWHM of the zero loss peak, in the electron energy loss spectroscopy (EELS) is 0.5 eV. HAADF STEM
454 images are acquired with a 27 mrad beam semi-convergence angle, inner and outer semi-collection
455 angles of 43 and 170 mrad, and with 22 pA beam current. STEM-EELS acquisitions are performed with
456 120 pA beam current, 33 mrad semi-collection angle into the GIF, combined with 0.05 eV/channel
457 energy dispersion. Dual EELS is performed to reposition the energy scale in all spectra. The EELS data
458 in Fig. 3 is taken in a single 820 nm long line which is then split into three 200 nm wide regions, as
459 indicated in Fig. 2, that are spatially averaged to give the spectra presented in Fig. 3. For measuring Er
460 displacement, series of fast/short-exposure HAADF-STEM images are acquired and processed with
461 SmartAlign⁴⁵. Atom plane detection is done with Atomap⁴⁶ and averages are computed based on all
462 planes.

463 **Density functional theory** DFT calculations are performed with the projector augmented wave (PAW)
464 method⁴⁷ as implemented in VASP^{48,49}. $3 \times 3 \times 1$ supercells with 270 atoms are used, with expected
465 $\text{Mn}^{2+}/\text{Mn}^{4+}$ concentrations of 3.70 %, to mimic the measured concentrations. For Y, Mn and O, 11, 11
466 and 6 electrons, respectively, are treated as valence electrons, with a plane-wave energy cut-off of
467 550 eV. Brillouin zone integration is done on a Γ -centered $1 \times 1 \times 2$ k -point mesh for geometry
468 optimizations, and on a $2 \times 2 \times 3$ mesh for density of states (DOS) calculations. **The DOS calculations have**
469 **an energy resolution of 0.0067 eV/point.** The non-collinear magnetic structure of the Mn sublattice is

470 approximated by a collinear frustrated antiferromagnetic order⁵⁰. Experimental lattice parameters⁵¹
471 and band gap⁵² are reproduced using the PBEsol functional⁵³ and spin-polarized GGA+U⁵⁴ with a
472 Hubbard U of 5 eV on Mn 3d. In defect cells ionic positions are optimized under fixed bulk lattice
473 parameters until the forces on all ions are below 0.01 eV Å⁻¹. Charge corrections for charged defects
474 in periodic boundary conditions are accounted for by extrapolation based on the Madelung
475 potential⁵⁵. As the electronic properties of oxygen stoichiometric¹⁹ and non-stoichiometric^{21,22} h-
476 RMnO₃ are governed by the bonding between Mn(3d) and O(2p) states, we choose the prototypical
477 h-YMnO₃ as our DFT model system to avoid f-electrons and slow convergence with Er.

478 **EELS simulations** A 30 atom unit cell is used as the input files in FEFF. Theoretical EELS (on
479 approximately 115 atom clusters) spectra are simulated using the FEFF9 code^{38,56} based on Green's
480 function multiple-scattering theory where the parameters SCF (specifies the radius of the cluster for
481 full multiple scattering during the self-consistency loop) and FMS (computes full multiple scattering
482 within a sphere of radius r centred on the absorbing atom) are set to certain values. An SCF of 4 Å,
483 FMS of 6 Å, and RPA screened corehole card is used for all clusters. In the EELS option card, the
484 following values are utilized from experiment: 200 kV beam energy, collection angle of 66.9 mrad,
485 convergence angle 27 mrad, and taken at the zone-axis [1 0 0] ($k_x=1, k_y=0, k_z=0$). A broadening of 0.5
486 eV is applied to account for the finite resolution in the EELS experiment, corresponding to the FWHM
487 of the zero loss peak (ZLP) in the EELS spectra.